Distinct predatory behaviors in scimitar- and dirk-toothed sabertooth cats

Borja Figueirido[1*], Stephan Lautenschlager[2], Alejandro Pérez-Ramos[1] and Blaire Van Valkenburgh[3*]

[1]Universidad de Málaga, Departamento de Ecología y Geología, Facultad de Ciencias, 29071-Málaga, Spain.
[2]School of Geography, Earth and Environmental Sciences, University of Birmingham, Edgbaston, Birmingham, B15 2TT, UK.
[3]Department of Ecology and Evolutionary Biology, UCLA, 621 Charles E Young Drive South, Los Angeles, CA 90095-1606.

Lead contact: Blaire Van Valkenburgh, bvanval@ucla.edu

*corresponding authors: Borja.figueirido@uma.es; bvanval@ucla.edu

Keywords: cranial biomechanics, cortical bone, trabecular bone, finite element analysis, paleobiology, killing bite, dirk-tooths, scimitar-tooths

SUMMARY

Over the Cenozoic, large cat-like forms have convergently evolved into specialized killers of 'megaherbivores' that relied on their large, and laterally-compressed (saber-like) canines to rapidly subdue their prey [1-5]. Scimitar- and dirk-toothed sabertooths are distinct ecomorphs that differ in canine tooth length, degree of serration, and postcranial features indicative of dissimilar predatory behavior [6-13]. Despite these differences, it is assumed that they used a similar 'canine-shear' bite to kill their prey [14,15]. We investigated the killing behavior of the scimitar-toothed *Homotherium serum* and the dirk-toothed *Smilodon fatalis* using a comparative sample of living carnivores and a new quantitative approach to the analysis of skull function. For the first time, we quantified differences in the relative amount and distribution of cortical and trabecular bone in coronal sections of skulls to assess relative skull stiffness and flexibility [16-19]. We also use finite element analysis to simulate various killing scenarios that load skulls in ways that likely favor distinct proportions of cortical versus trabecular bone across the skull. Our data reveal that *S. fatalis* had an extremely thick skull and relatively little trabecular bone, consistent with a large investment in cranial strength for a stabbing canine-shear-bite. However, *H. serum* had more trabecular bone, and likely deployed an unusual predatory behavior more similar to the clamp-and-hold technique of the lion than *S. fatalis*. These data broaden the killing repertoire of sabertooths and highlight the degree of ecological specialization among members of the large carnivore guild during the Late Pleistocene of North America.

RESULTS

Profiles of cortical and trabecular bone

As cortical bone tends to have high stiffness and trabecular bone has greater flexibility [16-19], we hypothesize that if dirk-tooths and scimitar-tooths had distinctive killing bites that loaded their skulls differently, they should diverge in the quantity and distribution of cortical and trabecular bone as well. For example, portions of the skull subjected to repeated or sustained loads that vary in direction, such as when holding struggling prey, would benefit from having a

greater proportion of trabecular bone, whereas those that suffer very peak, unidirectional loads would benefit from a greater proportion of cortical bone (see discussion). To test this, we quantified the relative amount of cortical and trabecular bone of complete skulls of the two sabertooths and three extant large carnivores, African lion (*Panthera leo*), spotted hyena (*Crocuta crocuta*), and African wild dog (*Lycaon pictus*) (Figure 1A; see methods for justification of comparative sample). Our results reveal that the skulls of all species show two clear peaks in cortical bone surface area relative to the total area of the skull (RCBT) to varying degrees with the exception of the wild dog (Figure 1B, left). The first lies at the upper fourth premolar (carnassial, slice #5), and the second at the temporomandibular joint (TMJ, slice #8). In the wild dog, the peak at the carnassial is not pronounced, and cortical bone area increases more gradually across the skull than in the feliforms (Figure 1B, left). Across all five species, there is considerable variation in the distribution of cortical bone surface area across the skull, with *S. fatalis* exceeding all species in the snout (slices #1-5; Figure1B; Figure 2) except at the anteriomost point of the upper carnassial, where it is surpassed by the spotted hyena (slice #3; Figure 1B). The snout of *H. serum* has values of relative cortical bone area that are below those of *S. fatalis* except at slice #1, the most anterior point of the canine, and also is very similar at slice #5, the most posterior point of the upper carnassial. Between those two positions, the snout of *H. serum* is more similar to that of the extant lion in relative compact bone surface area and much less than observed in the hyena and *S. fatalis*. (Figure 1B, left). Beyond slice #5, both saber-tooths have similar values of cortical bone that fall below those of the wild dog and hyena posteriorly (slices #5-10; Figure 1B).

On a per slice basis, the proportion of cortical bone surface area relative to the total area per slice fluctuates across the skull in all five species, with all showing a decline at the TMJ (slice #8, Figure 1C, left). Within the snout, the proportion of cortical bone surface area relative to the total area per slice is greatest in the spotted hyena and *S. fatalis*, and least in the lion and *H. serum* (Figure 1C, left). Interestingly, the snout of the wild dog is similar to that of the spotted hyena and *S. fatalis* in the proportion of compact bone at two anterior locations (slices #2-3), but then declines for the remainder of the snout (slices #4-5; Figure 1C, left).

Trabecular bone surface area relative to total skull area in *S. fatalis* is most similar to that of the spotted hyena, and to a lesser extent, *H. serum* and the wild dog (Figure 1B, right). The lion stands out with an unusually large proportion of trabecular bone at the TMJ (slice #8, Figure 1B; Figure 2) as well as higher values at both the posterior margin of the upper carnassial/frontal region and behind the TMJ (slices #4-5, 9-10; Fig 1B). The relatively large proportion of trabecular bone in the lion is confirmed in the analysis of trabecular bone surface area relative to the total area per slice, in which the lion displays an exceptionally large proportion of trabecular area per slice at the TMJ and caudal most position. (slice #8, 10, Figure 1C). On a per slice basis, the values for *H. serum* are also elevated and similar to those of the lion within the anterior-most part of the snout (slices # 1-3; Figure 1C). However, posteriorly (slices # 4-10; Figure 1B), *H. serum* has relative trabecular bone area per slice values within the range of *S. fatalis* and all extant species except the lion (slices # 5-10; Figure 1B).

Finite element analysis

We used 3D biomechanical modelling to simulate divergent killing scenarios, such as stabbing or pulling back, that load skulls differently and therefore are likely to favor distinct proportions of cortical and trabecular bone across the skull. Biomechanical function and efficiency of the models were assessed via von Mises stress and displacement magnitudes. Von

Mises stress is a scalar function of principal stresses (along orthogonal planes) and is a good predictor of ductile material failure (20), whereas displacement magnitude indicates the deformation of individual elements/regions due to external loading.

A comparison of von Mises stress values for each species under the four different loading scenarios reveals that the skulls of the three felids undergo less stress during stabbing bites than the skulls of either *Crocuta* or *Lycaon* (blue line, Figure 3A). Within the felids, *S. fatalis* exhibits the least stress during a stabbing bite, followed closely by *H. serum* and then lion. However, average values of node displacements under a stabbing load are very similar for both sabertooths (Figure 3B).

Contour plots of von Mises stress distributions reveal notable differences between *S. fatalis* and *H. serum* during bilateral canine stabbing and pulling back. During bilateral canine stabbing, both sabertooths show relatively high stress across their braincase that differs anteriorly, with *S. fatalis* exhibiting less stress across the rostrum than *H. serum* (Figure 4). This also is confirmed when simulating the combined action of the stabbing external force and the jaw closing muscles (Figure S2A). However, the situation differs during the pull-back scenario, in which both show similar stress in the rostrum but *S. fatalis* has greater stress across the braincase and zygomatics than *H. serum*. All three of the extant species experience higher stresses during bilateral canine stabbing than either of the sabertooths with and without the addition of active jaw adductors (Figure 4, Figure S2A).

Mean von Mises stress values in *S. fatalis* (Figure 3A) under laterally directed extrinsic loads (lateral shake) are greater than in any other simulated scenario, and exceed those observed for either *H. serum* or the lion. In both the lion and *H. serum*, stresses are similar and the laterally directed extrinsic forces largely concentrate von Mises stress within the zygomatics and rostral region, but the lion's snout is less stressed than that of *H. serum* (Figure 4). However, average values of node displacement under lateral shake loads indicate that *H. serum* experiences considerably lower displacements than the lion or *S. fatalis* (Figure 3B).

All the taxa experience lower average von Mises stress values with a jaw-muscle-driven bite (Figure 3A), but this is particularly true for the skull of *C. crocuta* and *L. pictus* (Figure 3A). Stresses are lower in this scenario than the others because the primary forces are distributed across the braincase and posterior half of the skull, and the rostrum is relatively unaffected (Figure 4). In contrast, because the extrinsic scenarios focus the loads on the rostrum, the skulls are more prone to bending, especially in elongated skulls.

In the second intrinsic scenario (i.e., jaw adductors plus neck muscles), all taxa experience higher levels of von Mises stress (Figure S2B) because the skulls are overloaded relative to the first intrinsic scenario (without neck muscles). Among the felids, *P. leo* is the most stressed, followed by *H. serum,* and then *S. fatalis*.

DISCUSSION

Cortical bone has a higher Young's modulus than trabecular bone, and therefore greater supportable load per unit of surface area. Cortical bone also has a lower strain index and thus greater stiffness and ability to resist torque (16-19). Consequently, the large amount of cortical bone in the rostrum of *S. fatalis* (Figure 1B; Figure 2) indicates that, similar to the bone-cracking spotted hyena, it was better equipped to resist larger and more localized stresses than the rostra of both *P. leo* (Figure 1B; Figure 2) and the scimitar-toothed *H. serum* (Figure 1B,C; Figure 2). In fact, the 3D simulations of different killing-bite scenarios reveal that the rostrum of *S. fatalis* was better able to withstand loads induced when stabbing prey than that of *H. serum* (Figure 4).

Moreover, within our sample of five carnivorans, only the skull of *S. fatalis* exhibits lesser displacement under a stabbing than lateral-shake scenario (Figure 3B).

Unlike cortical bone, trabecular bone has a lower Young's modulus, and a reduced supportable load per unit of surface area, but thus has a higher strain index that gives it greater flexibility (16-19). Moreover, trabecular bone exceeds cortical bone in resisting compression and shear (16-19). The small proportion of trabecular bone in *S. fatalis' skull* (Figure 1B, C; Figure 2), particularly posteriorly, suggests that it was not optimized for resisting sustained, multidirectional and large loads imposed by struggling prey (Figure 3; Figure 4). As demonstrated by previous researchers (e.g., 21), *S. fatalis* probably used its powerfully-built forelimbs (10,22) with hypertrophied dew claws (23,24) to bring down and fully immobilize large prey, and then applied one or two quick, strong killing-bites to the throat (e.g., 1,2, 7, 13, 14, 25, 26).

In contrast, the large amount of trabecular bone in the posterior region of the skull of *P. leo* (Figure 1B,C; Figure 2) reflects its ability to resist continuous and repetitive multidirectional loads that might occur during a prolonged 'clamp-and-hold' bite (27,28). Results of the FEA analyses also suggest that lion skulls are better adapted to resist laterally-directed loads than those of the sabertooths. For example, although both *P. leo* and *H. serum* exhibit similar levels of stress during a lateral-shake scenario (Figure 3A), the lion's rostrum is less stressed above the canines (Figure 4). Moreover, whereas *H. serum* experiences slightly lower levels of stress under stabbing than lateral-shake scenarios (Figure 3A), *P. leo* undergoes similar levels under both scenarios (Figure 3A), and the average skull displacement of *P. leo* was much lower under lateral-shake than stabbing scenarios (Figure 3B).

The quantity of cortical bone in the rostra of *H. serum* and *P. leo* are similar, but diverges posteriorly with *H. serum* exhibiting a greater proportion of cortical bone. However, relative cortical bone thickness at the TMJ remains less than that observed in *S. fatalis* (Figure 1B; Figure 2), suggesting that the scimitar cat's skull was subjected less often to peaks of locally concentrated and unidirectional forces than *S. fatalis*. The biomechanical simulations of bilateral canine stabbing support this suggestion, in that *H. serum* experienced levels of stress between that of *S. fatalis* and the three extant taxa (Figure 3B; Figure 4).

Like cortical bone, the fraction of trabecular bone is similar in the rostra of *H. serum* and *P. leo* (Figure 1B,C; Figure 2). And again, values of trabecular bone for *H. serum* fall between those of *P. leo* and *S. fatalis* behind the rostrum at most locations (Figure 1B,C; Figure 2). Therefore, *H. serum* probably possessed an intermediate ability to resist continuous and multidirectional loads relative to the other two felids. Again, the biomechanical simulations support this idea because the skull of *H. serum* and the lion display similar overall levels of stress under a lateral-shake scenario, and considerably less than *S. fatalis* (Figure 3A; Figure 4).

Consequently, *H. serum* likely deployed a predatory behavior among large felids not previously supported with quantitative data, that was in between the canine-shear-bite of *S. fatalis* (i.e, dirktooths) and the clamp-and-hold technique of lions (i.e., conical tooths). We argue that, like *S. fatalis*, multiple debilitating slashing bites to the throat of large prey was the likely predatory behavior for *H. serum*, and probably for all scimitar-tooths, as originally proposed by previous researchers based on qualitative assessments of morphology (e.g., 7). However, our results suggest that *H. serum* was less stressed than S. fatalis by laterally directed loads, which is consistent with a predatory behavior similar to that observed in the lion. Notably, an analysis of upper canine tooth bending strength in carnivorans found that the canines of *H. serum* also were

more resistant to bending and presumably fracture under mediolaterally directed loads than were those of *S. fatalis* (29).

The skull of the scimitar-tooth *cat* likely was able to support multidirectional loads incurred by struggling prey more often than was *S. fatalis* because of profound differences in forelimb morphology. Scimitar-tooths were somewhat cursorial predators in open habitats, whereas dirk-tooths behaved as ambush predators in more closed environments (11). The forelimbs of *H. serum* exhibit greater adaptations for speed, while those of *S. fatalis* emphasize adaptations for strength. Relative to *S. fatalis*, *H. serum* had less robust humeri (diameter/length), less broad humeral epicondyles, relatively shorter olecranon processes and a longer radius to humerus ratio, consistent with reduced mass and mechanical advantage of forelimb muscles (30). Although the claws of *H. serum* are compressed and curve-shaped, those of digits II-V are reduced and less retractile than those of *S. fatalis*, indicating an adaptive trade-off in the scimitar-tooth between improved traction for pursuing prey and enhanced grappling ability (31). All of these forelimb characteristics imply less reliance on forelimbs for immobilization of prey than in *S. fatalis*, and a consequent need for a craniodental skeleton better equipped to support lateral shaking (12). Therefore, our results suggest a gradient of functional adaptations within these highly specialized predators from the clamp-and-hold technique of the lion through *H. serum* to the exceedingly specialized canine-shear-bite of *S. fatalis.*

Based on the specimen we scanned, *S. fatalis* had an extremely thick skull as evidenced by coronal sections as well as quantitative measures (Figure 1). The combined thickness of cortical and trabecular bone (Figure S4), as well as cortical bone alone (Figure 1B,C), in the rostrum far exceeds that of any the other four species. *S. fatalis, H. serum* and the spotted hyena exhibit greater relative and total bone thickness at the TMJ than the lion (Figure S4), and unlike the lion, much of this thickness is cortical rather than trabecular bone. Spotted hyenas crack large bones with their strong teeth and jaws, and their massive TMJ likely reflects associated high bite forces (32, 33). Similarly, the extraordinary thickness of the rostrum and TMJ in *S. fatalis* suggests an unusually large investment in cranial strength, and argues for extremely high bite forces in this cat. Although our analyses were conducted on a single specimen and might not represent the pattern for the entire species, our results support clear differences in predatory behavior between the scimitar-tooth *H. serum* and the dirk-tooth *S. fatalis*. Given that previous studies document profound interspecific differences in locomotory and predatory strategies among saber-tooths (34), future studies including more species of living felines and other species of *Smilodon* and *Homotherium* (e.g., 35, 36), could provide additional insights into the diversity of cranial biomechanics in this intriguing group of extinct mammalian predators.

ACKNOWLEDGMENTS

We are grateful to Digimorph team, especially to Jessie Maisano for kindly providing the CTs analyzed in this study. Three anonymous reviewers and the Van Valkenburgh lab provided very helpful comments on the manuscript. Funding for this project was provided by the 'Spanish Ministry of Economy and Competitiveness (MINECO), grant (CGL2015-58300P) to BF. APR is a FPI fellow of the Spanish MINECO (BES-2013-065469) associated to the project (CGL2012-37866) of BF.

AUTHOR CONTRIBUTIONS

B.F., B.V.V. designed research; A. P.-R., B.F., S.L., B.V.V. performed research; B.F., B.V.V., A.P.-R., S.L., wrote the paper.

DECLARATION OF INTEREST

The authors declare no conflict of interest.

REFERENCES

1. Bohlin, B. (1940). Food habit of the machaerodonts, with special regard to *S. fatalis*. Bull. Geol. Inst. Upsala 28, 156-174.
2. Emerson, S.B., and Radinsky, L. (1980). Functional analysis of sabertooth cranial morphology. Paleobiology 6, 295-312.
3. Van Valkenburgh, B. (2007). Deja vu: the evolution of feeding morphologies in the Carnivora. Integr. Comp. Biol. 47, 147-163.
4. Andersson, K., Norman, D., and Werdelin, L. (2011). Sabretoothed carnivores and the killing of large prey. PLoS One 6, e24971.
5. Palmqvist, P., Martínez-Navarro, B., and Arribas, A. (1996). Prey selection by terrestrial carnivores in a lower Pleistocene paleocommunity. Paleobiology 22, 514-534.
6. Kurtén, B. (1968). Pleistocene Mammals of Europe. Weidenfeld and Nicolson, London.
7. Martin, L.D. (1980). Functional morphology and the evolution of cats. Transactions of the Nebraska Academy of Sciences 8, 141-154.
8. Slater, G.J., and Van Valkenburgh, B. (2008). Long in the tooth: evolution of sabertooth cat cranial shape. Paleobiology 34, 403-419.
9. Martin, L.D., Babiarz, J.P., Naples, V.L., and Hearst, J. (2000). Three ways to be a saber-toothed cat. Naturwissenschaften 87, 41-44.
10. Meachen-Samuels, J.A., and Van Valkenburgh, B. (2010). Radiographs reveal exceptional forelimb strength in the sabertooth cat, *S. fatalis fatalis*. PLoS one 5, e11412.
11. Anyonge, W. (1996). Locomotor behaviour in Plio-Pleistocene sabre-tooth cats: a biomechanical analysis. J. Zool. 238, 395-413.
12. Antón, M. (2013). Sabertooth. Indiana University Press.
13. Gonyea, W. J. (1976) Behavioral implications of saber-toothed felid morphology. Paleobiology 2, 332-342.
14. Akersten, W.A. (1985). Canine function in *S. fatalis* (Mammalia; Felidae; machairodontinae). Natural History Museum of Los Angeles County, Contributions in Science, 356.
15. Antón, M., and Galobart, A. (1999). Neck function and predatory behavior in the scimitar toothed cat *H. serum latidens* (Owen). J. Vertebr. Paleontol. 19, 771-784.
16. Carter, D.R., and Hayes, W.C. (1977). Compact bone fatigue damage—I. Residual strength and stiffness. J. Biomech. 10: 325-337.
17. Guede, D., González, P., and Caeiro, J.R. (2013). Biomecánica y hueso (I): Conceptos básicos y ensayos mecánicos clásicos. Revista de Osteoporosis y Metabolismo Mineral 5, 43-50.
18. Reddy, S., Dischino, M., and Soslowsky, L.J. (2009). Biomechanics-Part I. Bone Pathology, ed. Khurana J (Humana Press, New York), pp. 61-68.
19. Mostakhdemin, M., Amiri, I.S., and Syahrom, A. (2016). Introduction of Bone Study. Multi-axial Fatigue of Trabecular Bone with Respect to Normal Walking, eds. Mostakhdemin M, Amiri IS, Syahrom (Springer Singapore), pp. 1-4.

20. Dumont, E. R., Piccirillo, J., & Grosse, I. R. (2005). Finite-element analysis of biting behavior and bone stress in the facial skeletons of bats. *The anatomical record*, *283*(2), 319-330.
21. McHenry, C.R., Wroe, S., Clausen, P.D., Moreno, K., and Cunningham, E. (2007). Supermodeled sabercat, predatory behavior in *S. fatalis fatalis* revealed by high-resolution 3D computer simulation. P. Natl. Acad. Sci. USA 104, 16010-16015.
22. Martín-Serra, A., Figueirido, B., and Palmqvist, P. (2017). Non-decoupled morphological evolution of the fore-and hindlimb of sabretooth predators. J. Anat. 231, 532-542.
23. Cox, M., and Jefferson, G.T. (1988). The first individual skeleton of *S. fatalis* from Rancho La Brea. Current Research in the Pleistocene 5, 66-67.
24. Bryant, H.N., Russell, A.P., Laroiya, R., and Powell, G.L. (1996). Claw retraction and protraction in the Carnivora: skeletal microvariation in the phalanges of the Felidae. J. Morphol. 229, 289-308.
25. Antón, M., Salesa, M.J., Pastor, J.F., Sanchez, I.M., Fraile, S., and Morales, J. (2004). Implications of the mastoid anatomy of larger extant felids for the evolution and predatory behaviour of sabretoothed cats (Mammalia, Carnivora, Felidae). Zool. J. Linn. Soc.-Lond. 140, 207-221.
26. Salesa, M.J., Antón, M., Turner, A., and Morales, J. (2005). Aspects of the functional morphology in the cranial and cervical skeleton of the sabre-toothed cat *Paramachairodus ogygia* (Kaup, 1832) (Felidae, Machairodontinae) from the Late Miocene of Spain: implications for the origins of the machairodont killing bite. Zool. J. Linn. Soc.-Lond. 144, 363-377.
27. Schaller, G.B. (2009). The Serengeti lion: a study of predator-prey relations. University of Chicago Press.
28. Sunquist, M., and Sunquist, F. (2017). Wild cats of the world. University of Chicago Press.
29. Valkenburgh, B.V., and Ruff, C.B. (1987). Canine tooth strength and killing behaviour in large carnivores. J. Zool. 212, 379-397.
30. Meachen-Samuels, J.A. (2012). Morphological convergence of the prey-killing arsenal of sabertooth predators. Paleobiology 38, 1-14.
31. Antón, M., Galobart, A., and Turner, A. (2005). Co-existence of scimitar-toothed cats, lions and hominins in the European Pleistocene. Implications of the post-cranial anatomy of *H. serum latidens* (Owen) for comparative palaeoecology. Quaternary Sci. Rev. 24, 1287-1301.
32. Kruuk. H. (1972). The Spotted Hyena" a study of predation and social behavior. Chicago; Univ. Of Chicago Press.
33. Ravosa, M.J., Kunwar, R., Stock, S.R., and Stack, M.S. (2007). Pushing the limit: masticatory stress and adaptive plasticity in mammalian craniomandibular jonts. J. Experimental Biology 210, 628-641.
34. Lewis, M.E., and Lague, MR. (2010). Interpreting sabertooth cat (Carnivora; Felidae; Machairodontinae) postcranial morphology in light of scaling patterns in felids. Carnivoran evolution: new views on phylogeny, form and function. Cambridge University Press, Cambridge, 411.
35. Lund, P.W. 1842. Blik paa Brasiliens Dyreverden för sidste Jordomvaeltning. Fjerde Afhandling: Forstsaettelse af Pattedyrene. Danke vidensk. Selsk., 9:137-209.

36. Rincón, A. D., Prevosti, F. J., & Parra, G. E. (2011). New saber-toothed cat records (Felidae: Machairodontinae) for the Pleistocene of Venezuela, and the Great American Biotic Interchange. *Journal of Vertebrate Paleontology*, *31*(2), 468-478.
37. Marinelli, W. (1938). Der Schlidel von *S. fatalis*, nach der Funktion das Kieferapparates analysiert. Paleobiologica 6, 246-272.
38. Rawn-Schatzinger, V. (1992). The scimitar cat, *H. serum serum* cope: osteology, functional morphology, and predatory behavior. Illinois State Museum.
39. Marean, C.W., and Ehrhardt, C.L. (1995). Paleoanthropological and paleoecological implications of the taphonomy of a sabertooth's den. J. Hum. Evol 29, 515-547.
40. Antón, M., Salesa, M.J., Galobart, A., and Tseng, Z. J. (2014). The Plio-Pleistocene scimitar-toothed felid genus *H. serum* Fabrini, 1890 (Machairodontinae, Homotherini): diversity, palaeogeography and taxonomic implications. Quaternary Sci. Rev. 96: 259-268.
41. Schneider, C.A., Rasband, W.S., and Eliceiri, K.W. (2012). NIH Image to ImageJ: 25 years of image analysis. Nat. methods 9, 671-675.
42. Kikinis, R., Pieper, S.D., and Vosburgh, K.G. (2014). 3D Slicer: a platform for subject-specific image analysis, visualization, and clinical support. Intraoperative imaging and image-guided therapy, ed, Jolesz FA (Springer New York), pp. 277-289.
43. Lehmann, L.A., Alvarez, R.E., Macovski, A., Brody, W.R., Pelc, N.J., Riederer, S.J., and Hall, Al. (1981). Generalized image combinations in dual KVP digital radiography. Med. Phys. 8, 659-667.
44. Ney, D. R., Fishman, E. K., Magid, D., and Drebin, R.A. (1990). Volumetric rendering of computed tomography data: Principles and techniques. IEEE Computer Graphics and Applications. 10, 24-32.
45. Cignoni, P., Callieri, M., Corsini, M., Dellepiane, M., Ganovelli, F., and Ranzuglia, G. (2008). Meshlab: an open-source mesh processing tool. Eurographics Italian Chapter Conference: 129-136.
46. Slater, G. J., and Van Valkenburgh, B. (2009). Allometry and performance: the evolution of skull form and function in felids. J. Evolution. Biol. 22, 2278-2287.
47. Chamoli, U., and Wroe, S. (2011). Allometry in the distribution of material properties and geometry of the felid skull: Why larger species may need to change and how they may achieve it. *Journal of Theoretical Biology*, *283*(1), 217-226.
48. Attard, M.R.G., Chamoli, U., Ferrara, T.L., Rogers, T.L., and Wroe, S. (2011). Skull mechanics and implications for feeding behaviour in a large marsupial carnivore guild: the thylacine, Tasmanian devil and spotted-tailed quoll. J. Zool. 285, 292-300.
49. Bourke, J., Wroe, S., Moreno, K., McHenry, C., & Clausen, P. (2008). Effects of gape and tooth position on bite force and skull stress in the dingo (Canis lupus dingo) using a 3-dimensional finite element approach. *PLoS One*, *3*(5), e2200.
50. Thomason, J.J. (1991). Cranial strength in relation to estimated biting forces in some mammals. Can. J. Zool. 69, 2326-2333.
51. Sezgin, M., and Sankur, B. (2004). Survey over image thresholding techniques and quantitative performance evaluation. J. Electron Imaging 13, 146-165.
52. Rayfield, E.J. (2007). Finite element analysis and understanding the biomechanics and evolution of living and fossil organisms. Annu. Rev. Earth Planet. Sci. 35, 541-576.

Figure 1. **Amount and distribution of cortical and trabecular bone.** A, *S. fatalis* skull (left); palatal view of the same skull showing the positions of the ten coronal slices selected for quantifying the area of cortical and trabecular bone (middle), and representative slice taken at position #8, the temporomandibular joint (right), with cortical bone in yellow and trabecular bone in green. B, Bivariate plots of cortical bone area relative to total skull area (RCBT) and trabecular bone area relative to total skull area (RTBT) across the ten coronal slices. C, Bivariate plots of cortical bone area relative to total area per slice (RCBS), and trabecular bone area relative to total skull area per slice (RTBS) across the ten coronal slices. See also Figure S4 for non-relativized areas of cortical and trabecular bone across the slices. The ten slices are: 1, anterior-most point of the canine; 2, posterior-most point of the canine; 3, anterior-most point of the fourth upper premolar; 4, junction between the metacone and paracone of the upper fourth premolar; 5, posterior-most point of the fourth upper premolar; 6, anterior-most point of the squamosal-jugal suture on the zygomatic arch; 7, posterior-most point of the squamosal-jugal suture on the zygomatic arch; 8, temporomandibular joint (TMJ); 9, anterior-most point of the tympanic bulla; 10, anterior-most point of the occipital condyles. The slices defined at interdental gaps are taken at alveolar margins. All the skulls are scaled isometrically to 200 mm from prosthion to inion. See also Supplemental Data and Figure S4.

Figure 2. **Selected coronal slices in the five large carnivores included in the sample scaled to the same maximum mediolateral width.** A, the dirk-toothed *S. fatalis fatalis*; B, the conical-toothed *Panthera leo;* C, the scimitar-toothed, *H. serum serum;* D, the spotted hyaena *Crocuta crocuta*; E, the African wild dog *Lycaon pictus*. Left shows coronal slice # 3, and right shows coronal slice #8. Cortical bone, yellow; trabecular bone, green. See also Supplemental Data.

Figure 3. Finite Element Analysis. A, average (per element) von Mises stress (MPa) for each species in a given loading scenario. B, Average nodal displacement (mm) of the models for each species in a given loading scenario as a proxy for model deformation. Data are for models under extrinsic and intrinsic loads during bilateral canine biting. See also Figure S1-S3.

Figure 4. **Von Mises stress contour plots obtained from Finite Element Analysis of the crania of both sabertooths and living carnivores under four loading conditions (stabbing, pull-back, lateral shake, and jaw-powered bite) during bilateral canine biting.** See also Figure S2 for the simulations of the extrinsic scenarios including the adductor muscles and a fifth intrinsic scenario considering jaw adductors plus neck muscles. In Figure S3 the results under unilateral canine biting are shown. See also Figure S1-S3.

STAR METHODS

CONTACT FOR REAGENT AND RESOURCE SHARING

Further information and requests for resources and reagents should be directed to and will be fulfilled by the Lead Contact, Dr. Blaire Van Valkenburgh (bvanval@ucla.edu).

EXPERIMENTAL MODEL AND SUBJECT DETAILS

The crania of the two extinct felids, *H. serum* and *S. fatalis*, as well as three extant carnivorans, African lion (*Panthera leo*), African wild dog (*Lycaon pictus*), and spotted hyena (*Crocuta crocuta*) were CT scanned. All specimens were adults as indicated by fully closed synchondroses

and complete tooth eruption. The three extant hypercarnivorous taxa were chosen because researchers have proposed that *H. serum* was more of a carrion-feeder than lion-like active predator (37-39), whereas others have suggested *H. serum* was more similar to pack-hunting canids (12) based on its more gracile limbs and lack of fully retractile claws (31, 40). All specimens were scanned at the University of Texas High-Resolution X-ray Computed Tomography Facility and the scans are available on the UT Digital Morphology website (www.digimorph.org).

The acquisition properties for *H. serum* were 1024x1024 pixel size for 16-bit TIFF images, 419 kV, 1.8 mA, with voxel size (mm) of 0.1904 (X), 0,1904 (Y), 0.6500(Z) (total slices = 495). The acquisition properties for *S. fatalis* were1024x1024 16-bit TIFF images, 420 kV, 1.8 mA, with voxel size in mm of 0.2143(X), 0.2143 (Y), 0.5000 (Z) (total slices = 629). The specimen of *S. fatalis* (LACMRLP R37376) is from Rancho La Brea (Los Angeles, California) collected at pit 91, and *H. serum* at (TMM 933-3444) was discovered at Friesenhahn Cave (Texas, USA).

We also used extant taxa for comparative purposes, as follows: (i) lion *Panthera leo* (MVZ 117849) of unknown sex as a large pantherine, specimen collected from Skukuza (Kruger Park, Tranvaal, South Africa), and scanned at the University of Texas High-Resolution X-ray CT (Facility Archive 0320), acquisition properties were 512x512 16-bit TIFF images of the whole skull, 420 kV, 1.8 mA, and the voxel size in mm was 0.5273(X), 0.5273 (Y), 1.0000 (Z) (total slices = 406); (ii) spotted hyena, *Crocuta crocuta* (UCMVZ 184551) as a bone-cracker model, a male collected from Masai Mara National Reserve, Kenya, and scanned at the University of Texas High-Resolution X-ray CT (Facility Archives 0277), acquisition properties were 512x512 16-bits and converted 8 bits TIFF images, 420 kV, 1.8 mA, with a voxel size in mm of 0.3242(X), 0.3242 (Y), 0.5000 (Z) (total slices = 528); (iii) African wild dog, *Lycaon pictus* (USNM 368441), as a pack-hunter hypercarnivore, a male collected in Bechuanaland, Makeleapudi, and scanned at the University of Texas High-Resolution X-ray CT, acquisition properties are 1024x1024 16-bit TIFF images, 419 kV, 1.8 mA, (total slices = 523).

Museum abbreviations are as follows: Museum of Vertebrate Zoology at University of California, Berkeley (UCMVZ); United States National Museum of Natural History at Washington DC (USNM); La Brea Tar Pits Museum, Los Angeles County, California (LCMRLP); and Texas Memorial Museum (TMM).

METHOD DETAILS

Segmentation of cortical and trabecular bone

The dataset for each of the scanned skulls consisted of a stack of 16-bit TIFF images, all of which were adjusted for brightness and contrast to eliminate background noise using ImageJ (41). All images were normalized at 0.5% and the histogram was adjusted to the range of interest (ROI) using the semiautomatic brightness/contrast tool of ImageJ (41). Subsequently, all images were converted to 8 bits and exported to 3D-slicer (42) to generate the 3D models of each skull. To select the total amount of bone, and to avoid possible overestimations due to Compton and photoelectric effects (43), we used a range of gray values of 70-255 and created a slice with all the bone. Subsequently, we manually added to this layer the relevant low density structures (e.g.,trabecular bone) using a range of grey values between 40-70. We decided to use this range of gray values in order to reach a compromise between capturing all the visible and very small trabeculae but avoiding: (i) the oversegmentation of the relevant bony structures; and (ii) the selection of other undesirable artifacts that are a result of Compton and photoelectric effects; and

(iii) the selection of non-relevant small particles. This resulted in a layer with all the information selected between 40-255 but excluding the background noise due to Compton and photoelectric effects (40). Using this layer, we then segmented cortical and trabecular bone, respectively, as those structures with gray values ranging from approximately 185-255 for cortical bone and 40-185 for trabecular bone.

For each 3D model of a skull, we selected ten 1-mm thick coronal slices at key points that were homologous in all the species (Figure 1A). Cortical and trabecular bone were segmented, respectively, in each of these ten slices excluding petrosal bones and teeth, based on the values of thresholding specified above using 3D-slicer (42). Thus, for each slice, we generated three independent layers, first for all bone, second for the cortical bone (yellow), and third for trabecular bone (green). Each layer was saved as a stack of TIFF images to be imported into imageJ (41). All the CTs were processed using a bicubic interpolation (44) in order to convert anisotropic voxels (in Z direction) to isotropic-sized voxels (the same X,Y,Z values). The stacks for each skull were scaled to a total length of 200 mm from prosthion to inion isometrically and oriented to this (reference) plane in imageJ (41).

For both fossil specimens, we used semi-automatic thresholding to select the grey values corresponding to the matrix (non-bony) material prior to selecting the ten coronal slices. The values for this thresholding varies across slices and depends upon the nature of matrix infilling. After selecting the slices, we manually segmented them to remove matrix still present inside the trabecular bone of the skull. Damaged trabeculae during the fossilization process in the skulls of both saber-tooths were not observed. Furthermore, the inclusion of the intra-trabecular spaces in the calculation of trabecular bone avoids possible (but not visible), very small damaged trabeculae. Therefore, there is not an appreciable potential impact of diagenesis on accuracy of measures of cortical and trabecular bone in both fossil skulls. Mirroring to compensate for missing structures was done in only a few instances. The exceptions were a few struts of the frontal sinus in *S. fatalis*, and a small portion of the palate of *H. serum*, that were restored by mirroring the preserved counterparts. Restored parts of the skull had a minimum potential impact on the calculation of cortical and trabecular bone across the skulls.

Both three-dimensional surface models were imported into MeshLab (45) in PLY or STL formats (Polygon File Format or the Stanford Triangle Format) for mesh repair, cleaning and simplification.

Finite Element Analysis

The 3D models of all skulls were imported into Hypermesh 11 (Altair Engineering) for the generation of solid meshes (consisting of approximately 1,000,000 tetrahedral elements per model) and the setting of boundary conditions. All skull models were scaled to the same surface area to allow comparisons of form and function independent of size (46). Material properties for bone and teeth were assigned in Hypermesh based on published values in comparable studies on mammalian carnivores (bone: E = 13.7 (cortical) & 9.29 (trabecular) GPa, $\upsilon = 0.30$, teeth: E = 38.6.0 GPa, $\upsilon = 0.4$) (46-48). All materials were treated as isotropic and homogenous. Teeth were assigned a single material property, as some of the CT data did not allow differentiating individual components (e.g.dentine, enamel). In the case of *S. fatalis*, the tips of the canines were reconstructed.

Five different functional scenarios were tested. Three extrinsic scenarios: (i) stabbing prey using both canine teeth with a dorsally directed extrinsic force of 500 N applied to the tips of both canines (stab in Figure 4); (ii) pulling the head posteriorly with both canine teeth

embedded in the prey and an extrinsic force of 500 N distributed over the posterior edge of the canines (pull-back in Figure 4); and (iii) shaking the head laterally while holding prey with both canine teeth and an extrinsic force of 500 N applied to the left side of both canines (shake in Figure 4). The extrinsic force (total of 1000 N for each scenario) was selected based on reported magnitudes for neck-muscle-driven bite force (21). For the extrinsic feeding scenarios, constraints were placed on the articular surface of the squamosal (five nodes on each side), as well as the occipital condyle (ten nodes) to restrain the model from movement in x-, y- and z-directions to simulate the fixed contact of the skull with other skeletal elements (i.e. mandible and vertebral column).

A further intrinsic scenario (iv) was analyzed that simulated a jaw adductor muscle-driven biting assuming a gape angle of 25 degrees following (49). For this purpose, jaw adductor muscle forces were estimated using the attachment area of each muscle (Figure S1), as a proxy for physiological cross-section area and multiplying it by an isometric muscle stress value of 0.3 N/ mm^2 (50). This approach likely underestimates the total muscle force and resulting bite forces due to simplifying a three-dimensional muscle volume to a two-dimensional surface area. However, given the lack of accurate data on muscle volume and architecture for fossil carnivorans, this approach provides a repeatable method for estimating muscle force across taxa and permits functional comparisons. Models in this scenario were constrained at the tip of the canine tooth (one node on each side) to restrain the model from movement in x- and y- direction (i.e. medial/lateral and anterior/posterior), but not in z-direction to simulate some penetration of the canines into the prey during biting.

Further to these scenarios and to simulate the combined action of the jaw adductor muscles and external forces (i.e., stab, pull-back, lateral shake) experienced during movement of the prey and/or the head, all extrinsic scenarios were also analyzed with adductor loads active.

In addition, a combined functional scenario (v) was tested simulating the combined action of the jaw closing muscles and the neck musculature. For this, an extrinsic force of 500 N on each side was added to the aforementioned intrinsic scenario and distributed over the back of the skull and the mastoid region. The magnitude of the load was selected to be the same as with the extrinsic scenarios, based on reported magnitudes for neck-muscle-driven bite force (21). The directions of the muscle forces were determined by creating vectors between the muscle origin and insertion sites, using corresponding mandibular models or simplified templates, where this was not possible (i.e. postcranial muscles).

Cranial (adductor) and postcranial muscles were considered separately in the functional analyses to evaluate their contribution to the stress behavior. However, combined loads of the cranial and postcranial musculature were tested as well (see supplemental Figure S2). Results show that the combined muscle forces have very little effect on the stress distribution. The simulations were performed during bilateral (Figure 3 and Figure 4) and unilateral (Figure S3) canine biting.

QUANTIFICATION AND STATISTICAL ANALYSES

Quantification of amount and distribution of cortical and trabecular bone

We converted the stacks into binary, and we used the plug-in of ImageJ, ‘analysing particles’ (51) to obtain the total surface area of cortical and trabecular bone (including intra-

trabecular spaces), respectively, in each slice. The segmented slices were all perpendicular to the reference plane.

The values of surface areas of cortical and trabecular bone were scaled by: i) the sum of cortical and trabecular bone of the ten slices (i.e., total area of bone quantified across the skulls); and (ii) the total area of cortical plus trabecular of each slice. Both approaches are complementary in the following way: the first approach shows not only the distribution of cortical and trabecular bone across the skull, but also the heterogeneous distribution of bone across slices; with the second approach the contribution of cortical or trabecular in each slice is shown without regard to the heterogeneous distribution of bone across the skull. All calculation were performed with Microsoft Excel.

The proportion of cortical to trabecular bone tends to decrease with increasing size among felids (47). Therefore, larger species have less cortical bone and more trabecular bone. However, this allometric effect does not affect our results, given that we analyzed the distribution of cortical and trabecular bone across ten functional key points of the skull, rather than just the total amounts of cortical and trabecular bone. Moreover, both *H. serum* (skull length=326mm) and *S. fatalis* (skull length=322mm) have skull sizes similar to that of the living lion (skull length=408mm), and yet they vary greatly in ratio of cortical and trabecular bone across their skulls.

Assesing biomechanical performance of FE models

All models were imported into Abaqus 6.141 (Simulia) for analysis and post-processing. Biomechanical performance for the FE models was assessed via contour plots of Von Mises stress distribution, reaction forces (52), and average Von Mises stress and displacement values per element with the top 1% of values removed to avoid the influence of individual stress singularities at constrained or loaded nodes.

DATA AND SOFTWARE AVAILABILITY

All data are provided in the Supplemental Information: Figures S1-S4. Supplemental Table S1 includes data related to Figures 1, 2 and STAR Methods. Data S1 is available in Dryad.

Data S1. Finite element models analyzed in this article. Related to Figures 1, 2, S1-S4, and Table S1.

Figure 1. Amount and Distribution of Cortical and Trabecular Bone

(A) *S. fatalis* skull (left); palatal view of the same skull showing the positions of the ten coronal slices selected for quantifying the area of cortical and trabecular bone (middle); and representative slice taken at position 8, the temporomandibular joint (right), with cortical bone in yellow and trabecular bone in green.

(B) Bivariate plots of cortical bone area relative to total skull area (RCBT) and trabecular bone area relative to total skull area (RTBT) across the ten coronal slices.

(C) Bivariate plots of cortical bone area relative to total area per slice (RCBS) and trabecular bone area relative to total skull area per slice (RTBS) across the ten coronal slices.

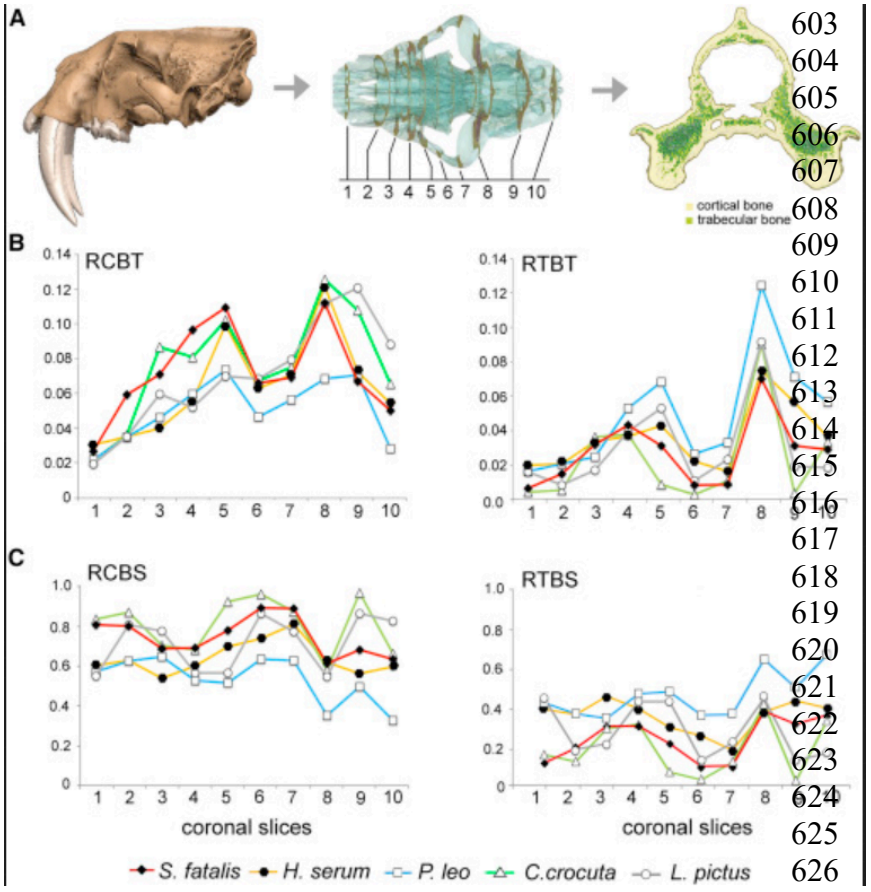

Figure 2. Selected Coronal Slices in the Five Large Carnivores Included in the Sample Scaled to the Same Maximum Mediolateral Width

The dirk-toothed *S. fatalis fatalis*m (A), the conical-toothed *Panthera leo* (B), the scimitar-toothed, *H. serum serum* (C),the spotted hyaena *Crocuta crocuta* (D), and the African wild dog *Lycaon pictus* (E). Coronal slice 3 is on the left, and coronal slice 8 is on the right. Cortical bone, yellow; trabecular bone, green. See also Table S1.

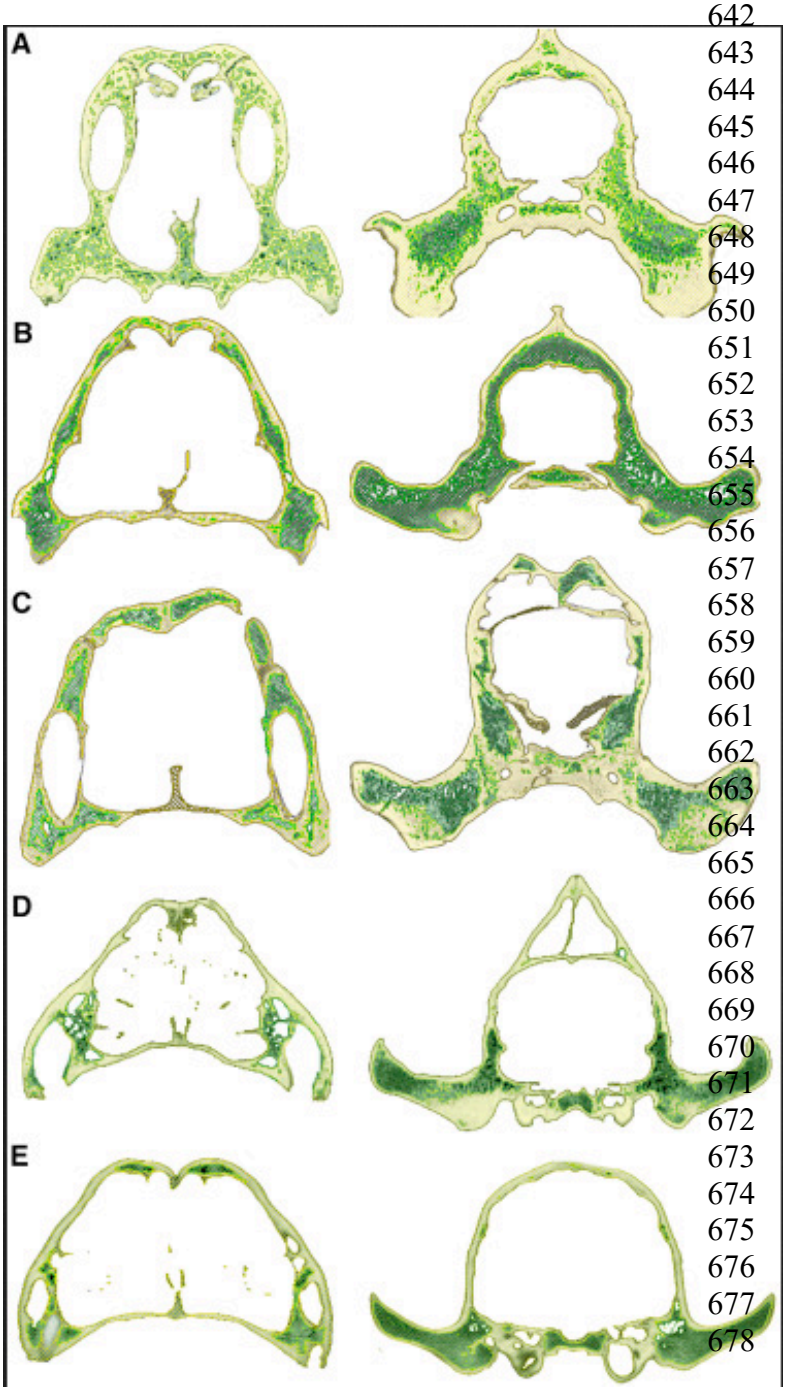

Figure 3. Finite Element Analysis

(A) Average (per element) von Mises stress (MPa) for each species in a given loading scenario.

(B) Average nodal displacement (mm) of the models for each species in a given loading scenario as a proxy for model deformation.

Data are for models under extrinsic and intrinsic loads during bilateral canine biting. See also Figures S1–S3.

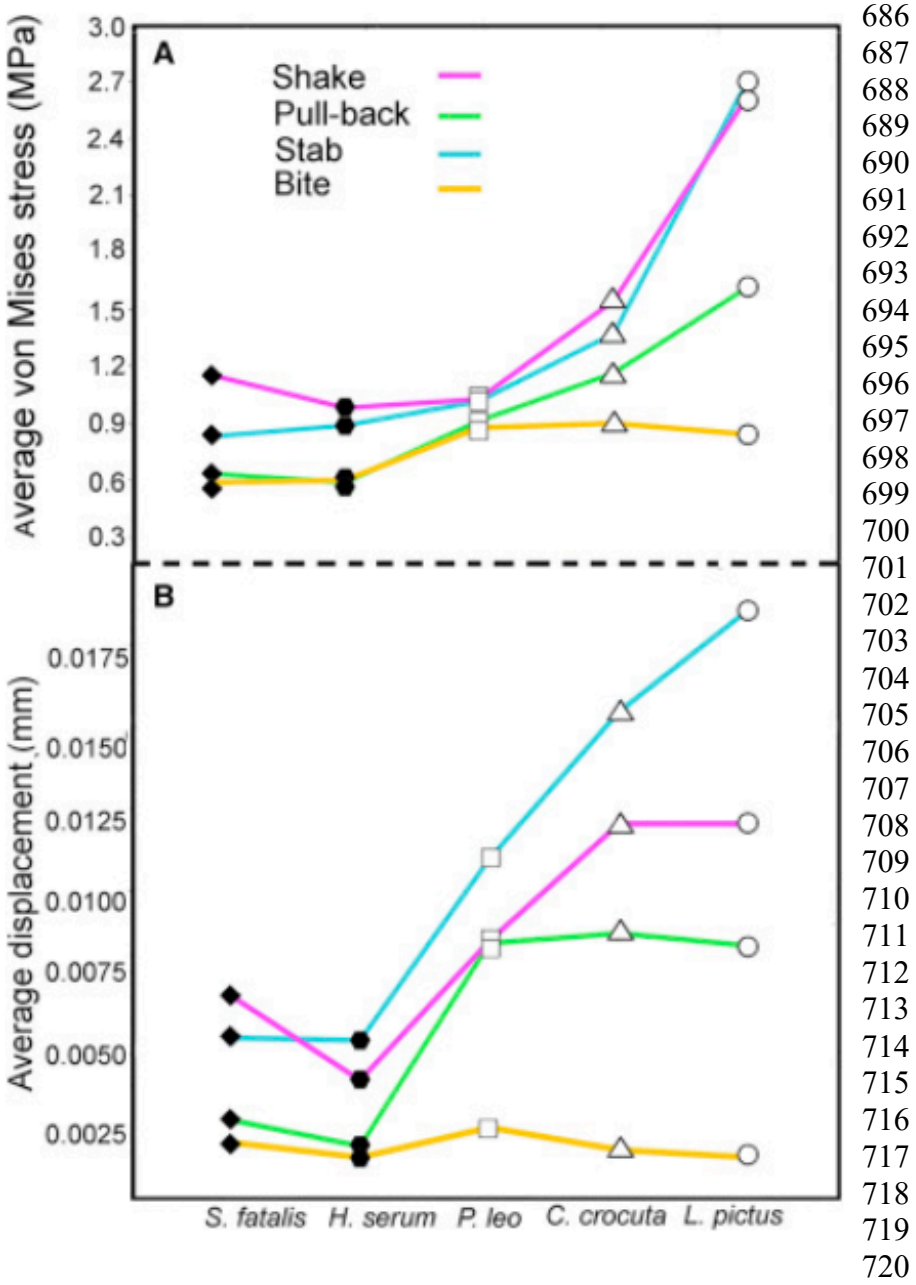

721 Figure 4. Von Mises Stress Contour Plots Obtained from Finite Element Analysis of the Crania
722 of Both Sabertooths and Living Carnivores under Four Loading Conditions—Stabbing, Pull-
723 Back, Lateral Shake, and Jaw-Powered Bite—during Bilateral Canine Biting